

FIG. 1.1. Location and type of events analyzed in this paper.

## 2. THE EXTRAORDINARY CALIFORNIA DROUGHT OF 2013/2014: CHARACTER, CONTEXT, AND THE ROLE OF CLIMATE CHANGE

DANIEL L. SWAIN, MICHAEL TSIANG, MATZ HAUGEN, DEEPTI SINGH, ALLISON CHARLAND, BALA RAJARATNAM, AND NOAH S. DIFFENBAUGH

*California's driest 12-month period on record occurred during 2013/14, and although global warming has very likely increased the probability of certain large-scale atmospheric conditions, implications for extremely low precipitation in California remain uncertain.*

*The event: 2013/14 drought in California.* Nearly the entire state of California experienced extremely dry conditions during 2013 (Fig. 2.1a). Statewide, 12-month accumulated precipitation was less than 34% of average (Fig. 2.1b), leading to a wide range of impacts. In early 2014, state and federal water agencies announced that agricultural water users in the Central Valley would receive no irrigation water during 2014 (DWR 2014; USBR 2014), and that a number of smaller communities throughout California could run out of water entirely within a 90-day window (USDA

2014a). Low rainfall, unusually warm temperatures, and stable atmospheric conditions affected the health of fisheries and other ecosystems (CDFW 2014), created highly unusual mid-winter wildfire risk (CAL FIRE 2014), and caused exceptionally poor air quality (BAAQMD 2014). Such impacts ultimately resulted in the declaration of a state-level “drought emergency” and the federal designation of all 58 California counties as “natural disaster areas” (USDA 2014b).

The California drought occurred in tandem with a highly persistent region of positive geopotential

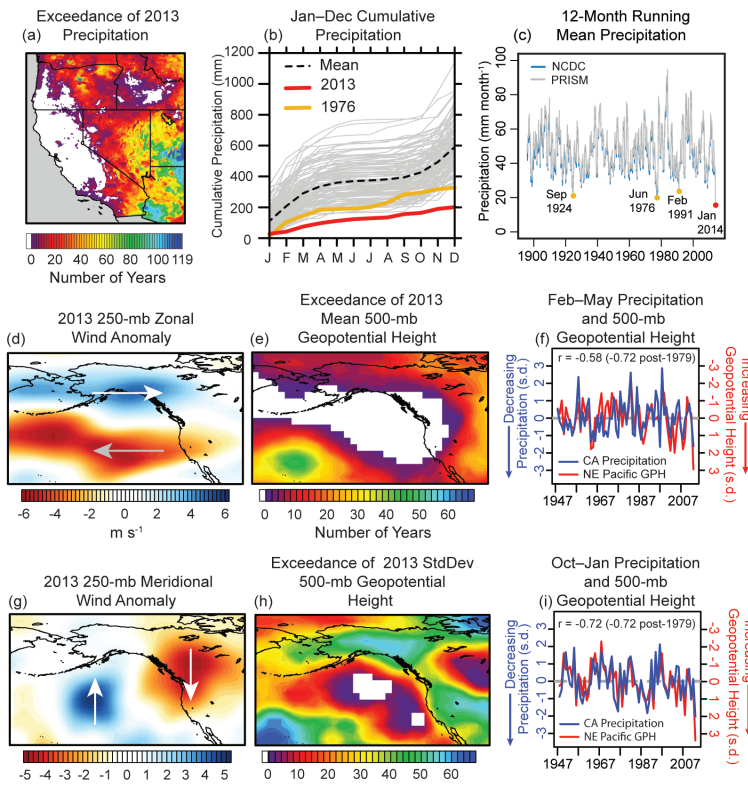


**FIG. 2.1. Structure and context of the 2013/14 event.** (a) Number of Jan–Dec periods during 1895–2012 in which precipitation was less than the Jan–Dec 2013 value, using the PRISM dataset. (b) Cumulative Jan–Dec precipitation in California for each year in 1895–2013, using the PRISM dataset. (The second-driest calendar year on record, 1976, is shown for reference.) (c) 12-month (one-sided) moving average precipitation in California from 1895 to 2014, using the NCLIMDIV (NCLIMDIV 2014) and PRISM (PRISM 2014) datasets. 12-month minima experienced during major historical droughts are highlighted. (d) Zonal and (g) meridional wind anomalies during Jan–Dec 2013. Arrows depict the direction of the primary anomaly vectors; the gray arrow in (d) denotes the region where easterly anomalies oppose mean westerly flow. (e) Number of Jan–Dec periods during 1948–2012 in which 500-mb GPH were higher than the Jan–Dec 2013 value. (f) Feb–May and (i) Oct–Jan normalized California precipitation (blue) and sign-reversed northeastern Pacific GPH (red) during 1948–2013 in NCEP reanalysis. (h) As in (e), but for standard deviation of daily 500-mb GPH.

height (GPH) anomalies over the northeastern Pacific Ocean (Fig. 2.1e,h), nicknamed the “Ridiculously Resilient Ridge” in the public discourse. Anomalous geostrophic flow induced by these highly unusual GPH gradients was characterized by weakened westerly zonal winds over the Pacific, strengthened zonal flow over Alaska (Fig. 2.1d), and a couplet of poleward-equatorward meridional wind anomalies centered in the northeastern Pacific around 135°W (Fig. 2.1g). This amplified atmospheric configuration displaced the jet stream well to the north, leading

to greatly reduced storm activity and record-low precipitation in California (Fig. 2.1a,b).

California typically experiences strong seasonality of precipitation, with the vast majority coinciding with the passage of cool-season extratropical cyclones during October–May (e.g., Cayan and Roads 1984). The meteorological conditions that occurred during what would normally be California’s “wet season”—namely, the presence of a quasi-stationary midtropospheric ridge and a northward shift/suppression of the storm track—strongly resembled the conditions during previous California droughts (Namias 1978a,b; Trenberth et al. 1988) and during extremely dry winter months (Mitchell and Blier 1997). The persistence of these meteorological conditions over the second half of the 2012/13 wet season and the first half of the 2013/14 wet season resulted in an extremely dry 12-month period (Fig. 2.1c).

*The 2013 event in historical context.* The 12-month precipitation and GPH anomalies are both unprecedented in the observational record (Fig. 2.1a,e). We find that a vast geographic region centered in the Gulf of Alaska experienced 500-mb GPH anomalies that exceeded all previous values (Fig. 2.1e) in the 66-year NCEP1 reanalysis (Kalnay et al. 1996). Standard deviation of the daily 500-mb GPH field was also extremely low over much of the northeastern Pacific (Fig. 2.1h), an indication of the profound suppression of

the storm track and of extratropical cyclonic activity induced by persistent ridging.

Likewise, most of California received less precipitation in 2013 than during any previous calendar year in the 119-year observational record (Fig. 2.1a). Observed precipitation over the 12-month period ending on 31 January 2014 was the lowest for any consecutive 12-month period since at least 1895 (Fig. 2.1c). Thus, the one-year precipitation deficit associated with the 2013/14 event was larger than any previous one-year deficit observed during California’s

historical droughts, including the notable events of 1976/77 and 1987–92.

One of the most remarkable aspects of the 2013/14 event was the spatial and temporal coherence of strong midtropospheric ridging and associated wind anomalies over multiple seasons. The spatial structure of observationally unprecedented GPH anomalies during both February–May 2013 and October–January 2013/14 was very similar to that of the 12-month mean (Supplementary Fig. S2.1), as was the structure of the ridging-induced anomalous flow. The coherence of this anomalous large-scale atmospheric pattern preceding and following the canonical June–September dry season was especially unusual. In particular, although high-amplitude meridional flow and positive GPH anomalies over the far northeastern Pacific are often associated with precipitation deficits in California (Carrera et al. 2004; Namias 1978a; Chen and Cayan 1994), the temporal resilience and spatial scale of the GPH anomalies were greater in 2013/14 than during previous droughts in California’s recent past (Fig. 2.1e).

#### *Quantifying the probability of a 2013-magnitude event.*

We define a “2013-magnitude event” as the mean January–December 2013 500-mb GPH over the core area of unprecedented annual GPH (35°–60°N and 210°–240°E; Fig. 2.1e). We find a strong negative relationship between northeastern Pacific GPH and California precipitation [for the 1979–2012 period, traditional correlation for February–May (October–January) =  $-0.72$  ( $-0.72$ ); Spearman’s correlation for February–May (October–January) =  $-0.66$  ( $-0.73$ ); Fig. 2.1f,i]. We use GPH to characterize the event based on the rarity of the GPH anomalies and the observed strength of the relationship between GPH and precipitation (Mitchell and Blier 1997; Chen and Cayan 1994). Because the 2013 12-month GPH fell far in the upper tail of the observational distribution (Fig. 2.2a), we calculate the likelihood of the 2013 event by fitting a Pareto III-type parametric distribution to the 1979–2012 reanalysis [Fig. 2.2a; Supplementary Materials (SM)]. We select the Pareto-III distribution for parametric fitting because it is characterized by a one-sided heavy tail, which allows for more stable estimates of return periods for extreme events occurring far in the upper tail of observed or simulated distributions (such as a 2013-magnitude event, see SM). We estimate that the return period for the 2013 12-month GPH value “likely” exceeds 285 years ( $>66\%$  confidence; Masstrandrea et al. 2011) and “very likely” exceeds 126

years ( $>95\%$  confidence), with a median estimate of 421 years (Fig. 2.2b).

We use the CMIP5 global climate models (Taylor et al. 2012) to compare the probability of persistently high GPH in the 20th century (20C) and preindustrial control (P.I.) climates (see SM). The relationship between northeastern Pacific GPH and California precipitation is well represented in the CMIP5 20C simulations (Langford et al. 2014). We select the 12 models for which 20C and P.I. GPH data are available, and for which the Kolmogorov-Smirnov goodness-of-fit test exceeds 0.2 between the climate model and reanalysis distributions (Supplementary Fig. S2.2). We find that the mean change in GPH between the P.I. and 20C simulations is positive for 11 of these 12 models (median change =  $+7.96$  m; Fig. 2.2d). We, thus, find large increases in the frequency of occurrence of events exceeding the highest P.I. percentiles in the 20C simulations (Fig. 2.2e). For instance, the median change in occurrence of GPH values exceeding the 99th P.I. percentile is  $>670\%$ . While the occurrence of events exceeding the P.I. 90–99th percentiles categorically increases in the 20C simulations (which include both natural and anthropogenic forcings), we find no such increase in those CMIP5 simulations which include only natural forcing (Fig. 2.2f; see SM). Thus, we find that anthropogenic forcing—rather than natural external forcing—dominates the simulated response in extreme GPH.

We also use the Pareto-III distribution to calculate the return period of the 2013-magnitude extreme GPH event in the CMIP5 simulations. Here we select the three CMIP5 models for which the Kolmogorov-Smirnov goodness-of-fit test exceeds 0.8 (i.e., the “B3” models; Supplementary Fig. S2.2). For these models, we again fit bootstrapped Pareto-III distributions to the simulated 20C (1979–2005) and P.I. distributions to estimate return periods for a 2013-like extreme GPH value in our index region (see SM). The distribution of ratios between the bootstrapped return periods calculated for the 20C and P.I. simulations suggests that it is “likely” (“very likely”) that the probability of extremely high GPH is at least a factor of 4.02 (2.86) as great in the current climate as in the preindustrial control climate (Fig. 2.2c). Although the trend in GPH during the 20C simulations strongly influences the increase in probability (Supplementary Fig. S2.3), we reiterate that the increased occurrence of extreme GPH does not occur in the absence of human forcing (Fig. 2.2f).

Because the spatial structure of the GPH field—rather than the regional mean value—is the ultimate

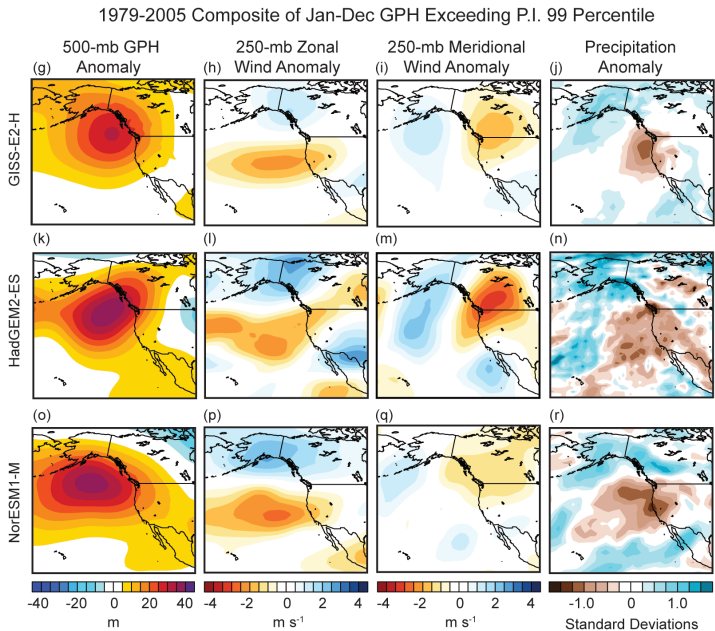
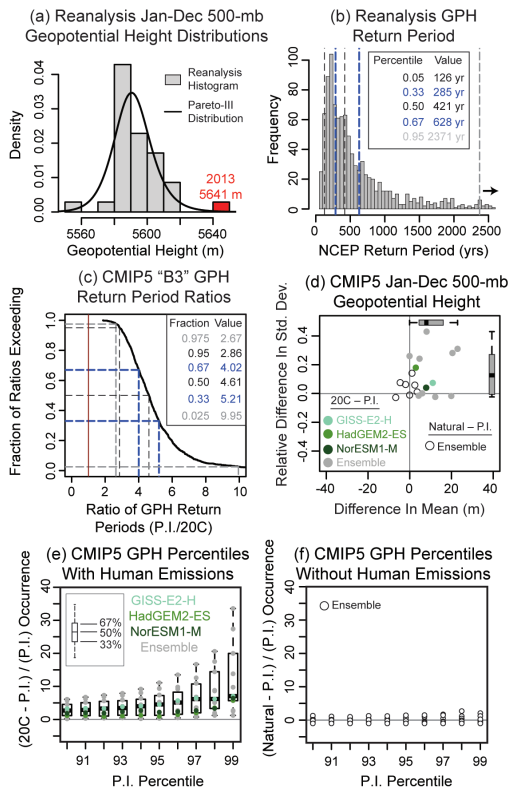


**FIG. 2.2. Quantifying the probability of a 2013-magnitude event. (a) Histogram (gray bins) and fitted Pareto-III distribution for NCEP reanalysis 500-mb GPH in the post-satellite period (1979–2013). The fitted distribution—shown for illustrative purposes—is estimated using the actual reanalysis distribution. (b) Distribution of bootstrapped return periods**

**for a 2013-magnitude Jan–Dec GPH event in the 1979–2012 reanalysis data. (c) Cumulative distribution of bootstrapped return period ratios for the preindustrial control (P.I.) and historical 20th century (20C) simulations in the B3 models, calculated as  $(P.I./20C)$ . (d) Absolute change in mean and relative change in standard deviation of 500-mb GPH in the historical 20C and natural forcing (“Natural”) CMIP5 simulations relative to P.I. B3 models are highlighted using green colors. (e) Frequency of exceedance of P.I. 0.90–0.99 500-mb GPH quantiles in the 20C simulations. (f) Frequency of exceedance of P.I. 0.90–0.99 500-mb GPH quantiles in the Natural simulations. (g–r) The composite 12-month anomaly fields, calculated for each of the B3 models, of 500-mb GPH (g,k,o), 250-mb zonal winds (h,l,p), 250-mb meridional winds (i,m,q), and total precipitation (j,n,r) from the 20C years in which the GPH in the North Pacific index region exceeds the respective P.I. 99th percentile.**

causal factor in rearranging the geostrophic flow field and shifting the midlatitude storm track away from California, we also examine the configuration of the large-scale atmospheric patterns associated with extreme GPH in the B3 models. For each of the B3 models, we composite the 12-month anomaly fields of 500-mb GPH, 250-mb winds, and total precipitation from each 20C year in which the GPH in our index region exceeds the respective P.I. 99th percentile. A zonally asymmetric pattern of positive GPH anomalies is apparent in all three model composites, with a distinct maximum located over the Gulf of Alaska region (Fig. 2.2g,k,o). This perturbation of the GPH field is associated with well-defined anticyclonic circulation anomalies, including weakened westerly flow aloft near and west of California (Fig. 2.2h,l,p) and enhanced equatorward flow aloft near the western coast of North America (Fig. 2.2i,m,q).

This composite spatial pattern strongly resembles the large-scale atmospheric structure that occurred during 2013 (Fig. 2.1d,e,g,h; Supplementary Fig. S2.2), and it is associated with large negative precipitation anomalies in the vicinity of California (Fig. 2.2j,n,r). These composite results thereby confirm that the extreme GPH events identified in our index region are associated with anomalous atmospheric circulation over the northeast Pacific and dry conditions in California.

We note two caveats. First, neither our probability quantification nor our compositing methodology quantifies the amplitude of extreme ridging events. Because we do not explicitly consider geopotential heights outside the North Pacific, it is likely that our inclusion of all years that exceed the 99th percentile P.I. GPH leads to inclusion of some events that have lower amplitude than that associated with either the

99th percentile P.I. GPH or the 2013 event. Thus, our present methodology cannot reject the possibility that the frequency of occurrence of years with anomalous GPH *gradients*—and the risk of extreme drought associated with a perturbed North Pacific storm track—has not changed between the preindustrial period and the present. [However, we note that Wang et al. (2014) do find evidence of increased high-amplitude ridging in this region in response to anthropogenic forcing.] Second, Neelin et al. (2013) report both an increase in long-term mean December–February precipitation over California and strengthened December–February mean westerly flow over the far eastern Pacific at the end of the 21st century under strongly increased greenhouse forcing (RCP8.5). These changes are opposite in sign to those associated with extreme annual GPH events in the 20C simulations relative to the P.I. control (Fig. 2.2).

*Conclusions.* The 2013/14 California drought was an exceptional climate event. A highly persistent large-scale meteorological pattern over the northeastern Pacific led to observationally unprecedented geopotential height and precipitation anomalies over a broad region. The very strong ridging and highly amplified meridional flow near the West Coast of North America in 2013/14 was structurally similar to—but spatially and temporally more extensive than—atmospheric configurations that have been previously linked to extreme dryness in Califor-

nia (Mitchell and Blier 1997; Namias 1978a,b). We find that extreme geopotential height values in this region, which are a defining metric of this type of atmospheric configuration, occur much more frequently in the present climate than in the absence of human emissions (Fig. 2.2).

The human and environmental impacts of the 2013/14 California drought were amplified by the timing of the event. The event began suddenly in January 2013, abruptly truncating what had initially appeared to be a wet rainy season following very heavy precipitation during November–December 2012 (DWR 2013). By persisting through January 2014, the event also effectively delayed the start of the subsequent rainy season by at least four months. The rapid onset and persistent high intensity of drought conditions presented unique challenges for decision makers tasked with making choices about the allocation of water to urban, agricultural, and environmental interests (USDA 2014a; DWR 2014). Together, the complexity and severity of the observed drought impacts, coupled with our finding that global warming has increased the probability of extreme North Pacific geopotential heights similar to those associated with the 2013/14 drought, suggest that understanding the link between climate change and persistent North Pacific ridging events will be crucial in characterizing the future risk of severe drought in California.

### 3. CAUSES OF THE EXTREME DRY CONDITIONS OVER CALIFORNIA DURING EARLY 2013

HAILAN WANG AND SIEGFRIED SCHUBERT

*The 2013 SST anomalies produced a predilection for California drought, whereas the long-term warming trend appears to make no appreciable contribution because of the counteraction between its dynamical and thermodynamic effects.*

*Introduction.* The state of California experienced extreme dry conditions during early 2013. In particular, January and February received 28% and 15%, respectively, of their normal monthly rainfall. When January and February are combined, January/February 2013 is ranked as the driest of the period 1895–2014. Such large precipitation deficits exerted enormous stress on water resources in an already

high water-demand region. Thus, it is of practical importance to investigate the causes of this extreme climate event so as to assess its predictability.

Climatologically, the winter precipitation over California comes from North Pacific storms that travel eastward under the guidance of the strong North Pacific jet stream. The oceanic storms transport abundant water vapor inland, with heavy

## S2. THE EXTRAORDINARY CALIFORNIA DROUGHT OF 2013/14: CHARACTER, CONTEXT, AND THE ROLE OF CLIMATE CHANGE

DANIEL L. SWAIN, MICHAEL TSIANG, MATZ HAUGEN, DEEPTI SINGH, ALLISON CHARLAND, BALA RAJARATNAM, AND NOAH S. DIFFENBAUGH

*Empirical analysis.* We calculate the probability of a 2013-magnitude event by analyzing the National Centers for Environmental Prediction reanalysis (NCEP1; Kalnay et al. 1996) and the Coupled Model Intercomparison Project Phase 5 (CMIP5) global climate model ensemble (Taylor et al. 2012). We define a “2013-magnitude event” as the mean January–December 2013 500-mb geopotential height (GPH) averaged over 35°–60°N and 210°–240°E, which emphasizes the area in which 2013 GPHs were unprecedented in the 66-year reanalysis (Fig. 2.1e in the main report; Fig.

S2.1). We justify the use of GPH to characterize the event given both the rarity of the GPH anomalies and the observed strength of the relationship between northeastern Pacific GPH and California precipitation (Fig. 2.1f,i in the main report; Mitchell and Blier 1997; Chen and Cayan 1994).

We restrict our probability analysis to the period from 1979 onwards, in order to focus on the satellite era, for which there is higher confidence in the accuracy of three-dimensional atmospheric fields in the reanalysis. Our CMIP5 model ensemble consists of 13

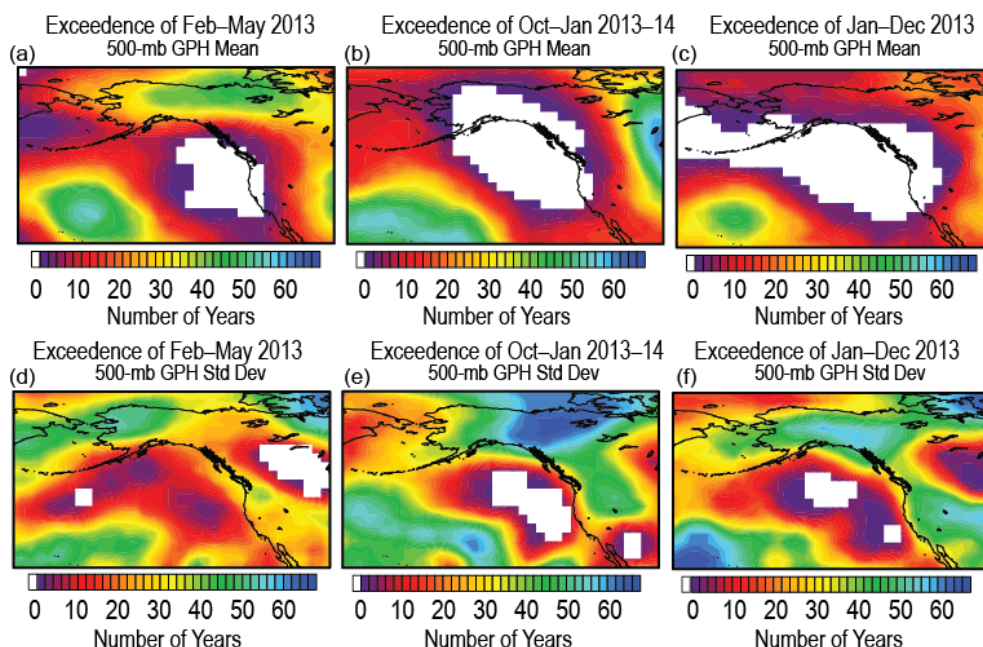


**FIG. S2.1.** Temporal and spatial structure of observationally-unprecedented 500-mb GPH in 2013–14. Shown are the number of Feb–May (a), Oct–Jan (b), and calendar year Jan–Dec (c) periods during 1948–2012 in which 500mb GPH exceeded the respective 2013 values. (d), (e), and (f) are the same as (a), (b), and (c), respectively, but for standard deviation of daily 500-mb GPH.

models for which GPH data are available for the long preindustrial control (pre-1850) simulations (Table S2.1). We compare the preindustrial (P.I.) simulation of each model with the 1979–2005 period of the 20th century (20C) simulations. (The CMIP5 20C simulations end in 2005.) We aggregate the 1979–2005 period from each model’s 20C realizations into a single 20C dataset for each model.

We first bias-correct the North Pacific 500-mb GPH data from each model by adjusting all simulated values by the difference between the NCEP1 reanalysis mean and the single-model mean:

$$GPH_{bias,corrected} = GPH_{model} + (\overline{GPH}_{reanalysis} - \overline{GPH}_{model}) \quad (1)$$

We then perform a Kolmogorov–Smirnov (K-S) test on each model to assess goodness of fit between the bias-corrected simulated distribution of annual 500-mb GPH and the reanalysis distribution. We find that the GPH distributions in one model (CCSM4; Fig. S2.2) are significantly different from the NCEP1 reanalysis at the  $p = 0.2$  level (i.e., agreement between the bias-corrected simulated distributions and the reanalysis distribution is poor). We, therefore, exclude CCSM4 from the remainder of our analysis.

To assess changes in the frequency of occurrence of extreme GPH values between the P.I. and 20C pe-

riods in each model, we first estimate the GPH value associated with each of the 90–99th P.I. percentiles (i.e., the P.I. 0.90–0.99 quantiles). We then count the number of times that a value equaling or exceeding this threshold occurs in the 20C simulations and calculate the relative change:

$$\Delta Freq = (Freq_{20C} - Freq_{PI}) / Freq_{PI} \quad (2)$$

**Parametric analysis of CMIP5 data.** We calculate the return period of the 2013-magnitude event by first finding a parametric distribution that is appropriate for both the reanalysis and CMIP5 data. In 2013, GPH fell far in the upper tail of the reanalysis record (and is clearly the most extreme event in the reanalysis time series; Fig. 2.2a in the main report). However, given the relatively short period of record for satellite-era observations, there is considerable uncertainty regarding the rarity of the event in a broader climate context. In order to provide a “lower bound” estimate on both the present-era probability of a 2013-magnitude event and the relative change in probability between a preindustrial control climate (absent the effect of anthropogenic forcing) and the historical period, we fit Pareto III-type distributions to the 1979–2012 reanalysis distribution and the 1979–2005 CMIP5 distribution (Fig. 2.2 in the main report). We use a Pareto distribution because of its characteristic heavy upper tail. The use of a heavy-tailed distribution means that our estimates for return periods associated with a 2013-like extreme upper-tail event are smaller than they would be if we had used a distribution with a more quickly attenuating tail, which is justified given the inherent uncertainty in both the true underlying distribution and in the selection of a parametric distribution. However, given the large variability of GPH and small sample size in the post-satellite era (Fig. 2.2a in the main report), we conduct extensive uncertainty quantification for both the reanalysis return period (Fig. 2.2b in the main report) and the CMIP5 20C and P.I. return periods (Fig. 2.2c in the main report; Fig. S2.3).

To find the three parameters in each Pareto III distribution, we graphically obtain the global maximum by examining the 3D empirical probability space given the observations. We then define a cube that surrounds the global minimum and sample from a uniform distribution with the graphically obtained bounds.

For fitting the Pareto to the CMIP5 simulations, we choose a restrictive “best 3” (B3) subset of CMIP5 models by selecting those models with

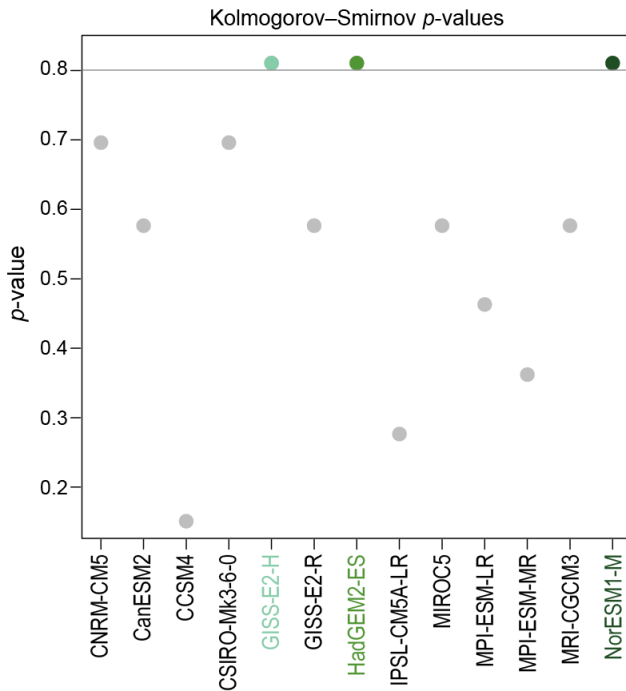


**FIG. S2.2.** Kolmogorov–Smirnov test results for each of the 13 CMIP5 models for which geopotential heights are archived for the P.I. simulations. Higher  $p$ -values suggest higher confidence that the mean-corrected model distributions match the NCEP reanalysis distribution. The B3 models are highlighted in green.

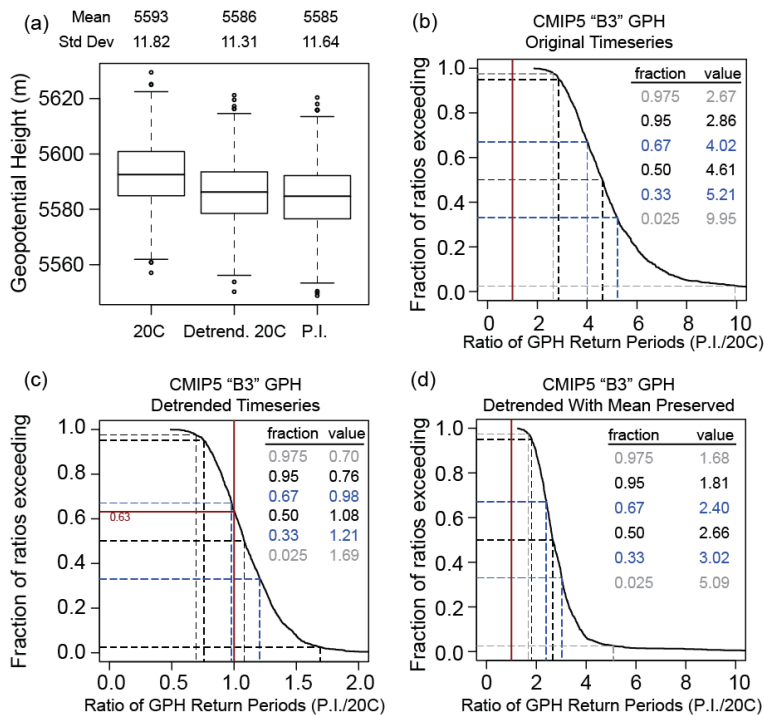


**FIG. S2.3. Impact of trend in GPH on distribution of return period ratios.** (a) Distribution of Jan–Dec GPH values in the pre-industrial control (P.I.) simulations of the B3 CMIP5 models, the historical 20th century (20C) simulations of the B3 CMIP5 models, and the detrended 20C simulations of the B3 CMIP5 models. (b) Cumulative distribution of bootstrapped return period ratios for the P.I. and 20C simulations in the B3 models, calculated as (P.I./20C). (d) As in Fig. S2.2b, but for detrended (c) and mean-preserved detrended (d) 20C simulations of the B3 CMIP5 models.

K-S test  $p$  values  $\geq 0.8$  (i.e., those models whose mean-corrected North Pacific GPH distributions are closest to the full NCEP reanalysis distribution, including the tails). The three models meeting this criterion are GISS-E2-H, HadGEM2-ES, and NorESM1-M (Fig. S2.2). We then aggregate the individual-model bias-corrected GPH values over all of the 1979–2005 model years from all 20C realizations of each of the B3 models. We then fit Pareto III distributions to this aggregate data in order to estimate the overall change in probability/shift in return period for a 2013-magnitude event.

To calculate the return periods in the CMIP5 B3 models, we first estimate the quantile of the 2013 event using the fitted NCEP distribution. We then find the magnitude of an event of the same quantile in the B3 20C simulations. We then estimate the probability of occurrence of an event of this magnitude in the B3 P.I. and 20C simulations. Finally, we calculate the associated return periods in the B3 P.I. and 20C simulations along with the ratio (P.I. divided by 20C).

*Uncertainty quantification for return period estimates.* To formally account for uncertainty in the parametric fitting and in the representativeness of the empirical distributions, we perform bootstrap resampling upon the original reanalysis distribution ( $B = 1000$ ) prior to fitting the Pareto III parametric distribution. The range of distributions and parametric fits resulting from the bootstrap allows us to quantify the uncertainty in the reanalysis return period for a 2013-magnitude event, including the “likely” (>66% confidence; Mastrandrea et al. 2011) and “very likely” (>95% confidence) range of values (Fig. S2.3b).

A bootstrap resampling methodology (with replacement) is also employed in fitting the P.I. control and historical 20C Pareto III distributions. In this analysis, all three distributions (reanalysis, P.I., and 20C) are simultaneously resampled and used to calculate return periods (and ratios of return periods). We note that the same parameter bounds are used in each iteration of the bootstrap. We report the resulting distribution of return period ratios (i.e., 1000 different estimates of the relative change in probability of a 2013-magnitude event between the P.I. and 20C forcing regimes) and again assign a “likely” and “very likely” range on the basis of the fitted distributions created using the resampled empirical distributions.

*Assessing the role of natural versus anthropogenic forcing in the late 20th century period.* We perform additional analysis using the CMIP5 20th century natural forcing (NAT) experiments and compare these results to those from the 20C historical experiments and from the P.I. control experiments (Taylor et al. 2012). The 20C simulations include both natural forcings (such as variability in solar irradiance and the inclusion of volcanic aerosols) and anthropogenic forcings (such as increasing concentrations of greenhouse gases), while the NAT experiments are identical to the 20C experiments except for the exclusion of anthropogenic forcings. The P.I. simulations assume constant solar irradiance, and include neither anthropogenic nor volcanic forcings.

We repeat our analysis of the empirical distribution of GPH in each model (described above) in order to determine the relative change in extreme (90–99th percentile) events between the different experiments. Although we find large increases in the frequency of occurrence of extreme GPH events in the 20C simulations relative to the P.I. simulations (Fig. 2.2e in the main report), we find little or no change in the probability of occurrence between the NAT and P.I. experiments (Fig. 2.2f in the main report). That the large simulated increase in the probability of extreme GPH events only occurs in climate model simulations that include natural and anthropogenic forcings and not in simulations that include only natural forcings suggests that the heightened probability cannot be explained without the anthropogenic contribution.

*Addressing the role of non-stationarity.* Our return period analysis—which requires fitting parametric models to reanalysis and climate model data—is predicated on a statistical assumption of stationarity in each time series. Because we find a statistically significant linear trend in the reanalysis time series, we take two separate approaches in detrending these data and performing additional analysis to quantify the role of the long-term trend in driving the simulated increase in probability of extreme GPH events in the CMIP5 models.

In the first approach, we detrend the reanalysis time series (excluding the extreme 2013 value) by fitting a linear model to the data and subtracting the accumulated trend at each point from the reanalysis

value. We then subtract the mean of the linearly detrended values and add the mean of the original time series:

$$GPH_{DTP} = (GPH_{DT} - \overline{GPH_{DT}}) + \overline{GPH_{original}} \quad (3)$$

The “detrended” 2013 value is defined as the difference between the actual 2013 value and its expected value in the linear model. We then perform an analogous operation on each 27-year 20C (1979–2005) realization from each of the B3 models to obtain mean-preserved, detrended time series. This approach yields a stationary series with the same mean as the original data, which we verify by analyzing the autocorrelation and partial autocorrelation structure of the new time series (using the Ljung–Box statistic). Our initial detrending approach controls for the existence of a linear trend in GPH over the reanalysis/20C period, but it does not remove the difference in the means between the 20C and P.I. periods. In this analysis, we find that the median P.I./20C ratio of extreme GPH probability is 2.66 (and is greater than 2.4 with 66% confidence and 1.81 with 95% confidence, respectively). While slightly lower than the non-detrended P.I./20C ratio, these results suggest that the simulated increase in the probability of extreme GPH is a statistically robust finding, even accounting for non-stationarity during the reanalysis/20C period.

In the second approach, we fit a linear model to the reanalysis time series (and each model realization) as before, but in this instance, we detrend the time

**TABLE S2.1. CMIP5 models used in Swain et al. 2014**

Model	piControl (rli p1) length (years)	Historical Number of Realizations	Natural Number of Realizations
CanESM2	996	5	5
CCSM4	501	8	—
CNRM-CM5	850	10	6
CSIRO-Mk3-6-0	500	10	5
GISS-E2-H	590	17	10
GISS-E2-R	850	23	—
HadGEM2-ES	280	5	4
IPSL-CM5A-LR	1000	6	3
MIROC5	670	5	—
MPI-ESM-LR	620	3	—
MPI-ESM-MR	990	3	—
MRI-CGCM3	500	5	1
NorESMI-M	501	3	—

series without preserving the original mean in each time series. This approach substantially reduces the difference in the mean between the CMIP5 20C and P.I. values (Fig. S2.3a). In this instance, we find that the P.I./20C ratio is much smaller than using either the original data or the mean-preserved detrended data (median value = 1.08), with error bars that make the trend statistically indistinguishable from zero (with 66% confidence that the ratio exceeds 0.98 and 95% confidence that the ratio exceeds 0.75; Fig. S2.3c). This result suggests that the linear trend in GPH over the 20C period has a substantial influence on the in-

crease in probability of a 2013-magnitude event that is simulated by the CMIP5 models. Given the modest simulated increase in GPH standard deviation (Fig. 2.2c in the main report) and the fact that the median of the second detrended distribution of P.I./20C ratios is positive [and the overall distribution is positively skewed (Fig. S2.3c)], there may be an additional contribution to the probability by nonlinear interactions (i.e., a trend in the variability). Further exploration of this possibility is beyond the scope of the present analysis, but will be the focus of future work.